‘Supplementary Information

Nonmetallic Plasmon Induced 500-Folds Enhancement in Upconversion Emission of UCNPs/WO_{3-x} Hybrid

Juan Li,[a] Weina Zhang,[b] Changhai Lu,[a] Zaizhu Lou[a] and Baojun Li*[a]*

[a]Institute of Nanophotonics, Jinan University, Guangzhou 511443, China
E-mail: zzlou@jnu.edu.cn, baojunli@jnu.edu.cn
[b]School of Materials Science and Engineering, Sun Yat-Sen University, Guangzhou 510275, China

1. The size distribution of the UCNPs.

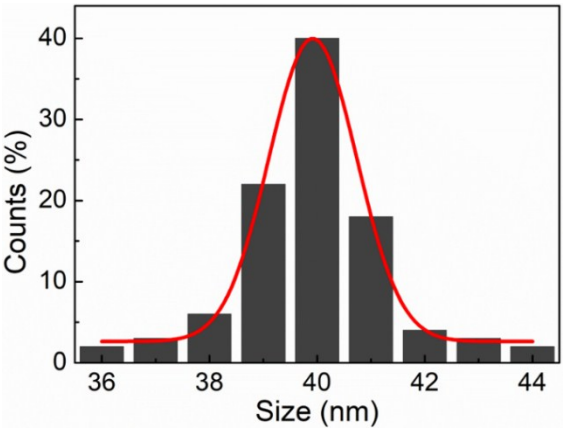

Fig. S1. The size distribution histogram of the UCNPs.

2. The normalized UCL spectrum of UCNPs.

Figure S2a presents the energy level diagram and energy-transfer upconversion process of UCNPs. Under 980-nm laser illumination, Yb^{3+} ions of the UCNPs were excited from the ground state $^2F_{7/2}$ to the $^2F_{5/2}$ state. Subsequently, the excited states of Er^{3+} ions ($^4F_{7/2}$, $^2H_{11/2}$, $^4S_{3/2}$, $^4F_{9/2}$ and $^4I_{11/2}$) are populated through a series of energy transfer from Yb^{3+} to Er^{3+} and a few nonradiative relaxation steps. Then, the electrons of Er^{3+} ions transited from the $^2H_{11/2}$, $^4S_{3/2}$, and $^4F_{9/2}$ states to the ground state, leading to visible emissions centered around 521, 540, and 654 nm respectively. Figure S2b shows the normalized UCL spectrum of UCNPs measured by a fluorescence spectrometer (FLS980, Edinburgh) equipped with a 980-nm laser.

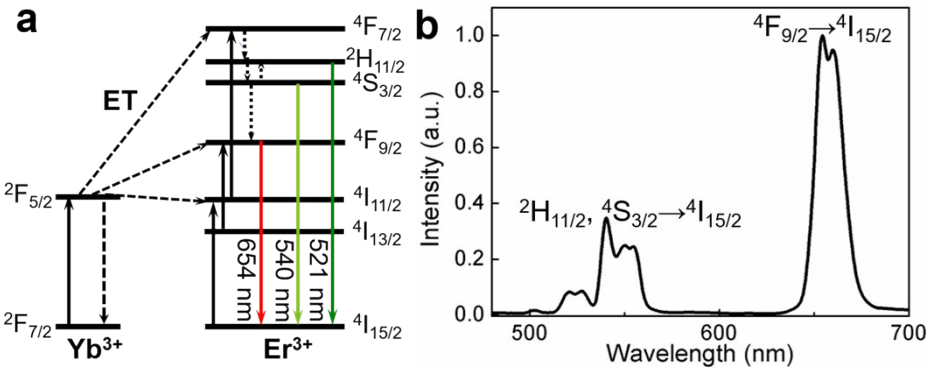

Fig. S2. The energy level diagram and energy-transfer upconversion process of UCNPs (a). The normalized UCL spectrum of UCNPs (b).

3. The characterization of plasmonic WO_{3-x} and UCNPs/WO_{3-x}.

Figure S3a shows the TEM image of plasmonic WO_{3-x}. The inset is the corresponding HRTEM image with a lattice fringe spacing of 0.38 nm. Figure S3b shows the XRD pattern of the UCNPs/WO_{3-x}, both the characteristic peaks of the UCNPs (indicated rhomboid) and WO_{3-x} (indicated by pentagon) are clearly observed. The peaks of UCNPs can be well indexed by the standard β-phase $NaYF_4$ (JCPDS No. 16-0334) while that of WO_{3-x} is consistent with (010) plane of monoclinic $W_{18}O_{49}$ (JCPDS No. 05-0392), revealing that the combination of them make no influence on their crystallinity.

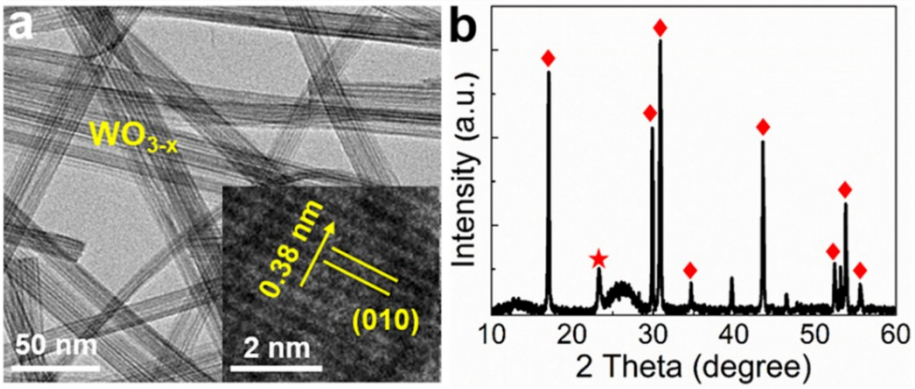

Fig. S3. The TEM image of plasmonic WO_{3-x} (a). The XRD pattern (b) of the UCNPs/WO_{3-x}.

4. The enhancement factors of UCNPs/WO_{3-x}

The samples of UCNPs/WO_{3-x} and UCNPs were excited with an incident laser power of 120 mW. Since the UC emission dependent more directly to the density of the excitation photon flux, an estimation of the power density of the 980 nm-excitation on the fiber surface was carried out as follows. At an incident laser source of 120 mW, the actual output power of a bare fiber without drawing treatment was measured as 98 mW by an optical power meter (OPHIR NOVA II). This power reduction is caused by the coupling and propagation loss of the fiber itself. With the same incident laser source, the actual output power of the optical fiber used in

experiment was further decreased to 16 mW, since a portion of light source (82 mW) was leaked out to excite the samples coated on the fiber surface. To simplify the calculation, the optical fiber coated with the sample was modeled as a cylinder with a surface area of 0.15 mm^2 (diameter of 9.4 μm and height of 5 mm) and the power density of the 980 nm-excitation on the fiber surface was estimated as ~55 W/cm^2. Figure S4 shows the enhancement factors (EFs) for different emissions, which is defined as the intensity ratios of UCNPs/WO_{3-x} to that of UCNPs with an incident laser power of 120 mW. The EFs for the emissions at 521, 540 and 654 nm are 540.1, 27.9 and 1.2, respectively.

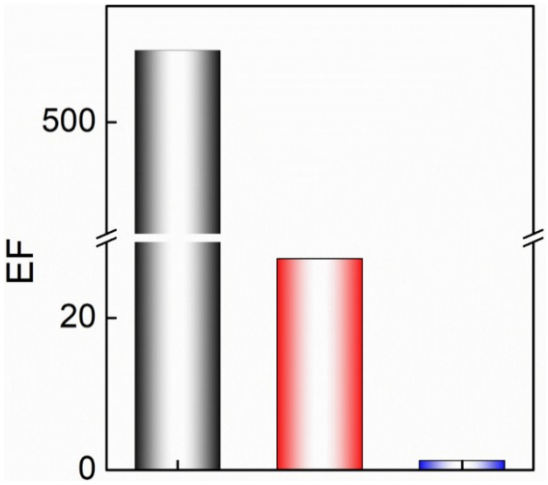

Fig. S4. The EFs for different emissions of UCNPs/WO_{3-x}

5. Photostability of the UCNPs/WO_{3-x}

To investigate the photostability of the UCNPs/WO_{3-x} hybrid, the sample was continuously excited with 980-nm laser power of 120 mW. As shown in Fig. S5, after continuous excitation of 5 min, the UCL intensity at 521, 540, and 654 nm emissions are decreased only 2.0, 4.3, and 5.9%, respectively, demonstrating the good photostability of the UCNPs/WO_{3-x} hybrid.

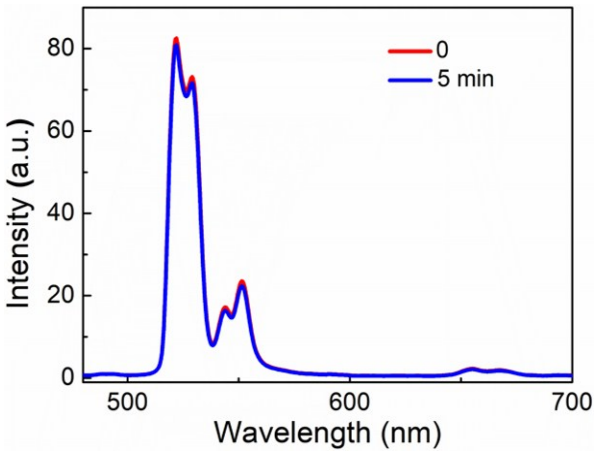

Fig. S5 The UCL spectra of the UCNPs/WO_{3-x} hybrid after continuous excitation of 5 min with 980-nm laser.

6. The calculated decay times τ

The UCL decay curves of UCNPs (hollow circle) and UCNPs/WO_{3-x} (solid sphere) at three characteristic emission peaks have been measured, as shown in Fig. S6. All of the decay curves can be fitted with a single exponential decay function

$$I = I_0 + A\exp(-x/\tau), \quad (1)$$

from which the decay time τ can be calculated (see Table 1).

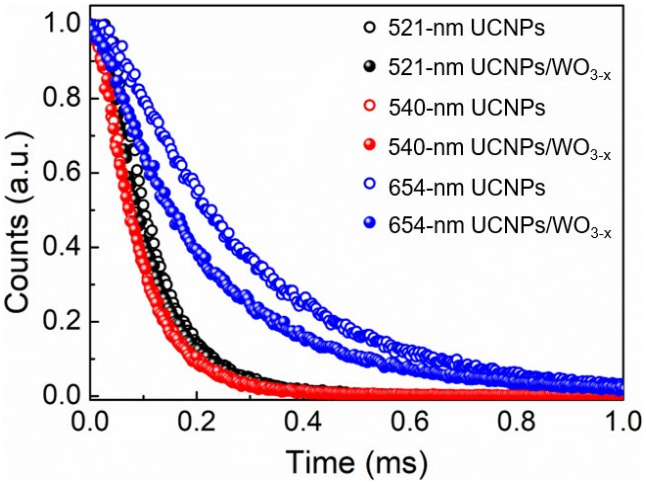

Fig. S6. The UCL decay curves of UCNPs (hollow circle) and UCNPs/WO_{3-x} (solid sphere) at three emission peaks fitted with a single exponential decay function.

Table 1. The calculated decay times τ

	τ_{521}(ms)	τ_{540}(ms)	τ_{654}(ms)
UCNPs	0.108	0.087	0.280
UCNPs/WO_{3-x}	0.098	0.085	0.210

7. Power-dependent UCL of UCNPs

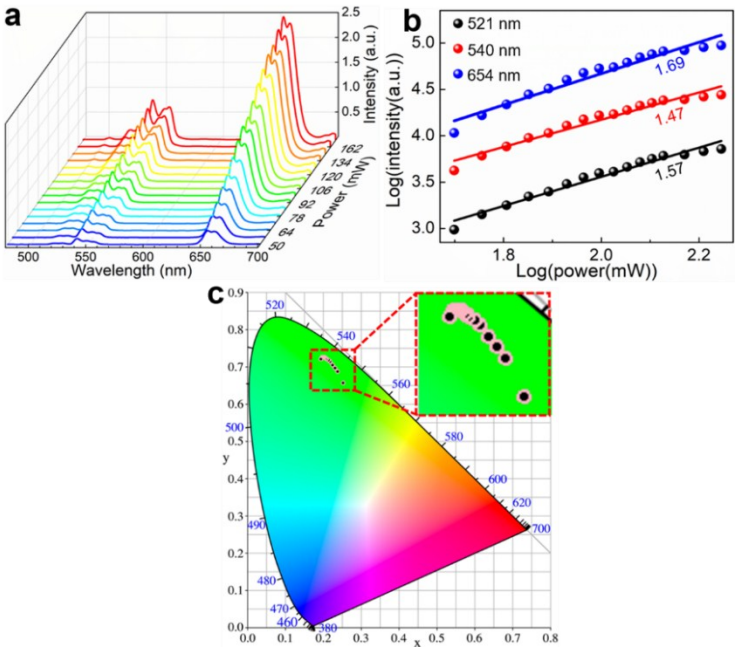

Fig. S7. The UCL spectra (a) of UCNPs under 980-nm laser excitation with varying powers from 50 to 176 mW. A plot of log(*I*) versus log(*P*) for the three peak emissions of the UCNPs (b). The power-dependent color coordinates of UCNPs/WO_{3-x} plotted in the CIE chromaticity diagram (c).

8. Power-dependent UCL spectra of the control samples

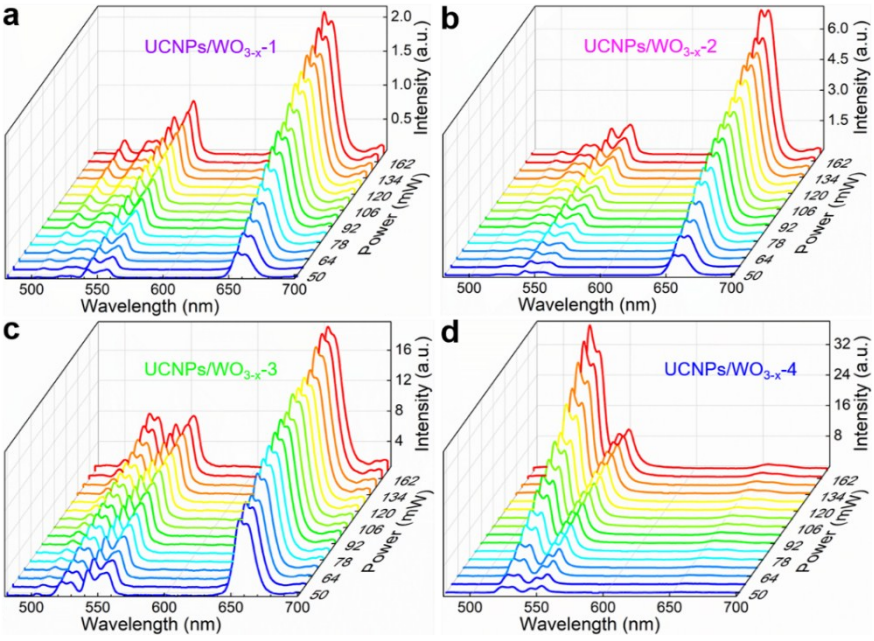

Fig. S8. The power-dependent UCL spectra of four control samples of UCNPs/WO_{3-x}-1(a), UCNPs/WO_{3-x}-2 (b), UCNPs/WO_{3-x}-3 (c) and UCNPs/WO_{3-x}-4 (d).

9. LSPR absoprtion-dependent of UCL

The EFs for 521-nm emission exhibit a quadratic increase with the increasing of plasmon absorption intensity of WO_{3-x}, as shown in Fig. S9a. Figure S9b show the power-dependent *IR* of I_{521}/I_{654} for different samples. It is clear that the I_{521}/I_{654} variation is negligible for the samples with non-plasmonic WO_{3-x}. With the emergence of WO_{3-x} plasmonic properties, the I_{521}/I_{654} value exhibit a significant increase, further demonstrating the plasmonic-induced selective enhancement. Figure S9c shows the CIE diagram at 120 mW laser power, visually presenting an obvious emission color variation of different samples.

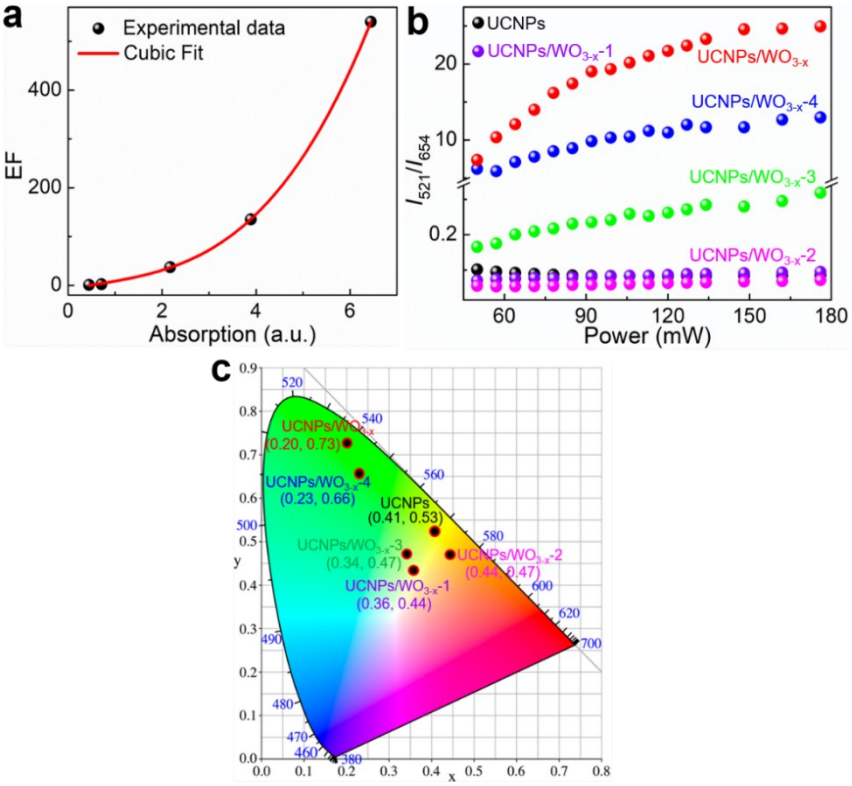

Fig. S9. The EFs variation for 521-nm emission as a function of the absorption intensity of WO_{3-x} (a). The power-dependent *IR* of I_{521}/I_{654} for different samples (b). The color coordinates of different samples at 120 mW laser power plotted in the CIE chromaticity diagram (c).

10. The UCL spectra of the UCNPs/PMMA/WO_{3-x}

To further demonstrate the selective UCL enhancement is mainly caused by the thermal effect, an additional sample with a polymer (Poly(methyl methacrylate), PMMA) insulation layer inserted between the UCNPs and the WO_{3-x} was fabricated. The WO_{3-x} samples were first treated by PMMA solution with a concentration of 20 mg/mL to form a PMMA spacer on the surface of WO_{3-x}. Then, the sample of UCNPs/PMMA/WO_{3-x} was coated on the optical fiber using the same method. In this case, the thermal effect was largely suppressed. Figure S10 shows the collected UCL spectra of the UCNPs/PMMA/WO_{3-x} and UCNPs samples at a laser power of 50 mW. Compared to the UCNPs, the UCL intensity enhancement factors of the

UCNPs/PMMA/WO_{3-x} sample are 1.6, 1.5 and 1.6 for 521, 540 and 655 nm emissions, respectively. Note that the enhancement factors are much lower and no selective enhancement phenomenon was observed. The former is due to that the increasing distance between UCNPs and WO_{3-x} weaken local field enhancement effect and the latter is caused by the suppressed thermal effect by the PMMA layer.

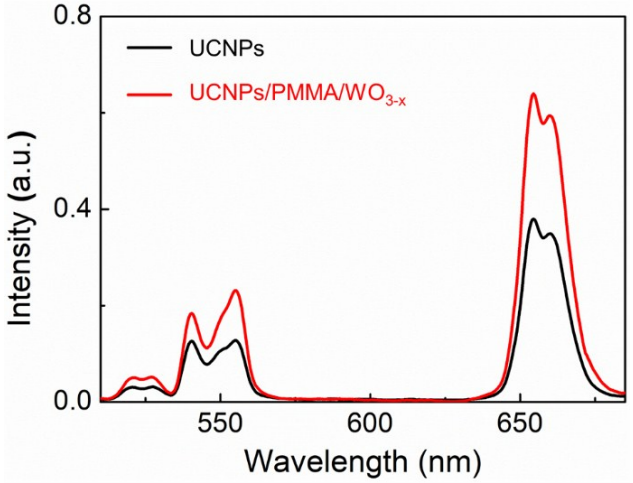

Fig. S10 The UCL spectra of the UCNPs/PMMA/WO_{3-x} and UCNPs samples

11. The ratiometric method

The selective enhancement in the UCL emission at 521 nm is mainly attributed to plasmonic WO_{3-x} induced thermal effect. The UCL emission at 521 and 540 nm come from the transitions of $^2H_{11/2}$, $^4S_{3/2} \rightarrow {}^4I_{15/2}$, respectively. The two emission intensities are proportional to the population of the corresponding energy levels ($^2H_{11/2}$ and $^4S_{3/2}$). At a certain temperature, the relative population of the $^2H_{11/2}$ and $^4S_{3/2}$ levels gets a thermal equilibrium and follows a Boltzmann distribution.

$$\frac{N_{521}}{N_{540}} = exp(-\frac{\Delta E}{k_B T}) \quad (2)$$

The intensity ratio (*IR*) of the two emissions at 521 and 540 nm (I_{521}/I_{540}) can be given by

$$\frac{I_{521}}{I_{540}} = \frac{N_{521} g_H \sigma_H \omega_H}{N_{540} g_s \sigma_s \omega_s} = Bexp(-\frac{\Delta E}{k_B T}) \quad (3)$$

which can be expressed as follows:

$$\ln(IR) = \ln B + \left(-\frac{\Delta E}{k_B T}\right) = \ln B + (-C/T) \quad (4)$$

Here, N and g are the population and the degeneracy of the excited levels, σ and ω are the spontaneous emission rate and the frequency of the transitions from the excited levels ($^2H_{11/2}$, $^4S_{3/2}$) to the $^4I_{15/2}$ level, respectively. ΔE is the energy gap between $^2H_{11/2}$ and $^4S_{3/2}$ levels, k_B is

the Boltzmann constant, B and C are constants to be determined, and T is the absolute temperature. Taken UCNPs as an example, the energy gap between the two levels is obtained from the UCL spectra ($\Delta E \approx 0.086$ eV) giving C value of 997 K. Figure S11 plots the linear fitted curve of IR versus the laser power, from which IR value at the limit of no laser power corresponding to 300 K can be extrapolated. Plugging these two values (IR = 0.215, T = 300 K) into equation (4), the value of ln$B$ is readily calculated as 1.786, consistent with the range of the constant (1.5-2.5) reported previously.[1]

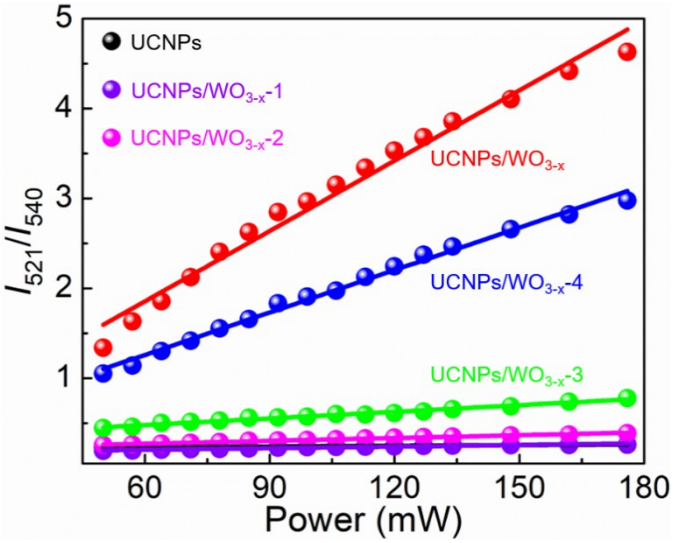

Fig. S11. The linear fitted curves of IR versus the laser power for different samples.

12. The XRD patterns.

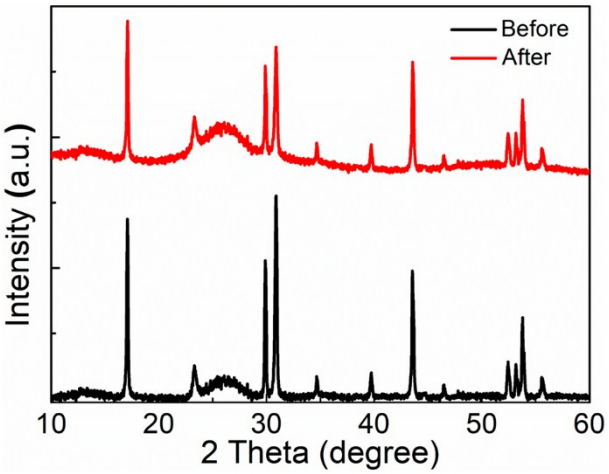

Fig. S12 The XRD patterns of the UCNPs/WO_{3-x} hybrid before and after the 980-nm laser irradiation.

13. The calculation of relative (absolute) sensitivity and temperature resolution

The relative sensitivity S_r is the change rate of IR vs temperature whereas the absolute sensitivity S_a is the IR variation along with temperature, which could be expressed as[2]

$$S_r = \frac{1}{IR}\frac{dIR}{dT} = \frac{\Delta E}{K_B T^2} \quad (5)$$

$$S_a = \frac{dIR}{dT} = IR\frac{\Delta E}{K_B T^2} \quad (6)$$

Another important parameter for temperature sensing is its temperature resolution, which is estimated by[3]

$$\delta T = \delta IR / S_a \quad (7)$$

Here, δIR is the resolution of IR, which can be calculated from the standard deviation of residuals in the polynomial interpolation/linear fit of the IR vs. T experimental data (Fig. S13).

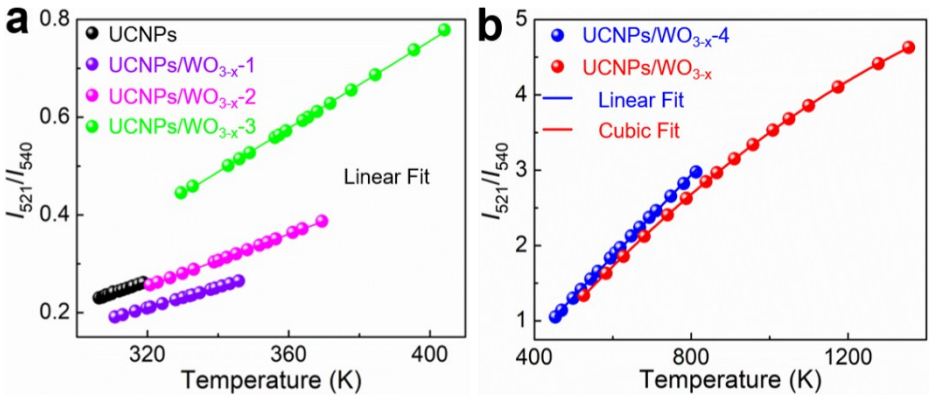

Fig. S13. The linear fitted curves (a) of IR vs. the temperature for samples of UCNPs, UCNPs/WO_{3-x}-1, UCNPs/WO_{3-x}-2 and UCNPs/WO_{3-x}-3, respectively. The linear fit/polynomial interpolation (b) of the IR vs. the temperature for samples of UCNPs/WO_{3-x}-4 and UCNPs/WO_{3-x}.

14. Summary of the parameters for different samples.

Table 2. Summary of the parameters for different samples

Samples	T (K)	S_a (10^{-4} K^{-1})	S_r (% K^{-1})	δT (K)
UCNPs	306-318	24.46-25.65	0.98-1.06	0.24-0.25
UCNPs/WO_{3-x}-1	310-345	19.75-22.07	0.83-1.03	0.17-0.18
UCNPs/WO_{3-x}-2	320-369	24.91-28.29	0.73-0.97	0.26-0.30
UCNPs/WO_{3-x}-3	329-404	40.90-47.54	0.61-0.92	0.48-0.56
UCNPs/WO_{3-x}-4	453-812	48.06-54.56	0.16-0.52	0.53-0.87
UCNPs/WO_{3-x}	525-1354	26.91-51.62	0.06-0.39	0.62-1.18

15. Comparison of temperature sensing parameters

Table 3. Comparison of temperature sensing parameters for reported Er^{3+} based up-conversion materials (Temperature range (ΔT, K), maximum relative sensitivity (S_m, % K^{-1}) and temperature resolution (δT, K)).

Material	ΔT (K)	S_m (% K^{-1})	δT (K)	Ref.
$NaYF_4$:Er^{3+}/Yb^{3+}/WO_{3-x}	**310−1354**	**1.03**	**0.17−1.18**	**our work**
$NaYF_4$:Er^{3+}/Yb^{3+}	298−318	1.00	---	[4]
$NaYF_4$:Er^{3+}/Yb^{3+}/Au film	333−811	1.46	2.9−3.0	[5]
$NaYF_4$:Yb^{3+}/Er^{3+}@Ag core/shell	293−303	---	---	[6]
Gd_2O_3:Yb^{3+}/Er^{3+}	300–900	0.73	---	[7]
GdOF:Nd^{3+}/Yb^{3+}/Er^{3+}@SiO_2	260−490	1.6	0.39−0.67	[8]
$(Gd,Yb,Er)_2O_3$-AuNPs-2.50	423−1050	0.72	2.0	[9]
ZnO: Er^{3+}	273–573	0.60	---	[10]
Er^{3+}/Yb^{3+}: $BaTiO_3$	322–466	0.41	---	[11]

16. The optical fiber

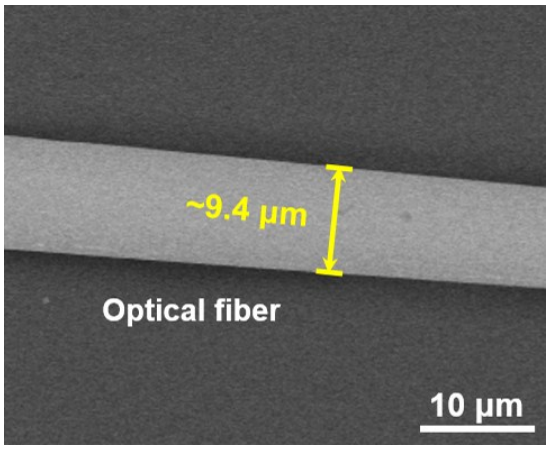

Fig. S14. The SEM image of the optical fiber with a diameter of ~9.4 μm.

Reference

1. T. Hayakawa, M. Hayakawa and M. Nogami, *J. Alloys Compd.*, 2008, **451**, 77.
2. H. Suo, X. Q. Zhao, Z. Y. Zhang and C. F. Guo, *ACS Appl. Mater. Interfaces*, 2017, **9**, 43438.
3. M. L. Debasu, D. Ananias, I. P. Santos, L. M. Liz-Marzán, J. Rocha and L. D. Carlos, *Adv.*

Mater., 2013, **25**, 4868.

4. F. Vetrone, R. Naccache, A. Zamarrón, A. J. de la Fuente, F. S. Rodríguez, L. M. Maestro, E. M. Rodriguez, D. Jaque, J. G. Solé and J. A. Capobianco, *ACS Nano*, 2010, **4**, 3254.
5. W. N. Zhang, J. Li, H. X. Lei and B. J. Li, *ACS Appl. Mater. Interfaces*, 2017, **9**, 42935.
6. B. Dong, S. Xu, J. Sun, S. Bi, D. Li, X. Bai, Y. Wang, L. P. Wang and H. W. Song, *J. Mater. Chem.*, 2011, **21**, 6193.
7. S. K. Singh, K. Kumar and S. B. Rai, *Sensor Actuat. A-Phys.*, 2009, **149**, 16.
8. H. Suo, X. Q. Zhao, Z. Y. Zhang and C. F. Guo, *ACS Appl. Mater. Interfaces*, 2017, **9**, 43438.
9. M. L. Debasu, D. Ananias, I. P. Santos, L. M. Liz-Marzán, J. Rocha and L. D. Carlos, *Adv. Mater.*, 2013, **25**, 4868.
10. X. Wang, X. Kong, Y. Yu, Y. Sun and H. Zhang, *J. Phys. Chem. C*, 2007, **111**, 15119.
11. D. Q. Chen, W. Xu, Y. Zhou and Y. Chen, *J. Alloys Compd.*, 2016, **676**, 215.